IEEE Access
Multidisciplinary ⋮ Rapid Review ⋮ Open Access Journal

Received 28 March 2024, accepted 11 April 2024, date of publication 18 April 2024, date of current version 30 April 2024.

Digital Object Identifier 10.1109/ACCESS.2024.3390932

RESEARCH ARTICLE

Development of a 3D Printed Structural Electronics Force Sensor

JUN XU, ZJENJA DOUBROVSKI, MEHMET OZDEMIR, JO M. P. GERAEDTS, AND YU SONG, (Member, IEEE)
Faculty of Industrial Design Engineering, Delft University of Technology, 2628 CE Delft, The Netherlands
Corresponding author: Jun Xu (j.xu-6@tudelft.nl)

The work of Jun Xu was supported by China Scholarship Council under Grant 201806890022.

ABSTRACT Structural electronics has garnered significant attention in the past decade. However, there remains a lack of a systematic approach in designing and manufacturing sensors that leverage both mechanical and electronic properties of materials for different applications. In this paper, we introduce a method for designing piezoresistive force sensors utilizing structural electronics and 3D printing techniques. Based on the principles of piezoresistive force sensing, we defined the geometric profile of the sensor by simultaneously maximizing strain and ensuring as uniform as possible stress distribution across the geometry. CAD models of the sensors were then formulated based on the optimized profile and fabricated using conductive filaments and the material extrusion 3D printing technique. Subsequently, we evaluated the accuracy, the sensitivity, and part-to-part variations of the sensors during loading and unloading. The influence of environmental temperature and humidity on the sensor's response were also investigated and compensated. Experiment results demonstrated the feasibility of the proposed method and revealed potential application domains, as well as limitations of the sensors.

INDEX TERMS Structural electronics, 3D printing, force sensor.

I. INTRODUCTION

Pressure sensors are of significance across a wide range of applications, spanning from robotic grippers [1], smart cushions [2] to wearables and digital twins [3]. Based on their operational principles, pressure sensors can be categorized into piezoelectric sensors, capacitance sensors, triboelectric sensors, and piezoresistive sensors [4], [5], [6]. Among these categories, the piezoresistive sensor has gained considerable attention due to its straightforward fabrication procedure, simplicity of the readout mechanisms, a wide detection range and sensitivity, rapid response time and low power consumption [7].

Most pressure sensors function as standalone components, e.g. in structural health monitoring [8] and wearables [9]. Researchers/engineers often require the flexibility to deploy these sensors in desired locations to meet various application requirements. At times, additional structures, such as fixtures, housings for wires, are required to support the functionality of these sensors. This introduces extra complexity into the design and manufacturing processes, leading to increased weight and costs. Structural electronics, which can integrate mechanical, electrical, and/or electronic components as part of a system [10], has demonstrated a novel approach to integrate electronic elements within the structures they are meant to serve. This results in lightweight, compact, and multifunctional devices.

In manufacturing of structural electronics, one way is to add conductive materials and electronics components on the structure where Laser Direct Structuring (LDS) and In-Mold Electronics (IME) are typical methods [11]. Another way is directly using dielectric and conductive materials in the construction of structure, e.g., via 3D printing. In this approach, the conductive material not only functions as mechanical structure, but also as conductive wires or even the sensing or actuating element [12]. For instance, Ntagios et al. developed a new design for a robot with an intrinsic sensing system printed by a multi-material

The associate editor coordinating the review of this manuscript and approving it for publication was Hassen Ouakad.

3D printer, enabling the robot to have advanced tactile sensing capabilities [13]. Goh et al. introduced an embedded resistive-based sensor and its design optimization was performed on the print pattern and the infill density to achieve the optimal sensitivity and repeatability [14]. Dijkshoorn et al. used multi-material printing and poly-jetting with FDM to demonstrate the effect with different printing orientations and infill patterns [15]. Laszczak et al. [16] developed a customized stress sensor based on a 3D-printed elastomeric frame, which is also addressed in Ni et al. [17] Another example is that Bao et al. introduced a double-robot 3D printing system for the fabrication of 3D structural electronics [18].

Conductive materials play a crucial role in 3D printed electronics. Silver paste was initially introduced for cold extrusion [11], [19]. However, the paste cannot be used to build structural components. An alternative strategy involves incorporating silver into various materials to create novel, printable composite materials. For example, Wei et al. developed a new type of hybrid Ag-coated nanofibers, resulting in the creation of 3D-printable, lightweight, and highly conductive nanocomposites [20]. In addition to silver, carbon particles and carbon nanotubes are also utilized in the development of 3D-printed materials, such as Proto-Pasta [21]. Mu et al. used commercially available acrylic-based UV-curable resin alongside multi-walled carbon nanotubes (MWCNTs) as primary constituents for Digital Light Processing (DLP) in 3D printing [22]. However, challenges such as cost, limited choices, suboptimal material characteristics, restricted colour options, and a lack of standardized certification remain associated with carbon-based 3D printing materials [23].

Using conductive materials and 3D printing techniques, researchers made significant efforts in designing and fabricating structural sensors [24], e.g. capacitive sensors based on conductive complex structures [22]. Another example is that Mata et al. developed printable sensors that can be used to assess sub-mT fields and can be bent to 2 mm bending radius without sacrificing the sensor magneto resistive performance [25]. Regarding force sensing, Guo et al. introduced a multi-functional strain sensor through a facile 3D printing technology [26]. However, to our knowledge, a systematic approach for designing structural electronic sensors while considering both mechanical and electronic requirements has not been proposed.

In this paper, we present the designing and manufacturing process of a structural electronics force sensor using 3D printing technique. The scientific contributions are:

- We propose a new computational design approach that designs the geometric shape of the structural electronics force sensor through optimization of a cost function that integrates both mechanical and electronic requirements;
- The designed force sensors were fabricated using 3D printing techniques. Subsequently, the sensors were characterized for accuracy, sensitivity, and part-to-part differences in both loading and unloading processes.

The remainder of this paper is organized as follows: Section II centres on detailing the geometric shape of the proposed sensor. In Section III, we describe the digital fabrication process. Section IV explores the characteristics of the structural electronic pressure sensor. Further insight into the proposed method, the sensor's properties and limitations are explored in Section V. Lastly, a short conclusion is drawn in Section VI.

II. SENSOR DESIGN

In this section, we introduce the proposed computational design approach, where we devised the geometry for the structural pressure sensor to ensure a more uniform stress distribution, thereby facilitating larger elastic deformation and increased capacity to withstand higher pressure. The optimization objective is to attain a broader working range and enhanced resolution.

The design of the sensor starts with a 2D symmetric contour shape. We have defined the initial contour as a single rectangular pulse shape, with additional vertices positioned at the left and right boundaries, respectively (Fig.1(a)). The lower part of the pulse shape serves as the support, while the upper part will bear the load. To increase the deformability of the sensor, we introduce extra degree of freedoms to both ''sides'' of the rectangular pulse shape, enabling the transformation to an ''S'' shape side wall while considering the reduction of space occupancy. Taken the left of the contour as an example, the geometry is defined based on points P_{LA}, P_{LB}, P_{LC}, and the $L_V = |P_{LA} - P_{LC}|$ and $L_H = |P_{RC} - P_{LC}|$, which are the vertical height of the pulse and the horizontal width of the pulse. Consequently, by introducing the tangents T_{LA}, T_{LB}, T_{LC} and points P_{LA}, P_{LB}, P_{LC}, we define a quadratic tangent curve B_L which is shown in Fig.1 (b) as:

$$B_L = C_T(P_{LA}, P_{LB}, P_{LC}, T_{LA}, T_{LB}, T_{LC}) \tag{1}$$

While the L_V and L_H can be specified by the user as the design requirement, and $P_{LB} = (P_{LA} + P_{LC})/2$, B_L can be denoted as:

$$B_L = C_T(T_{LA}, T_{LB}, T_{LC}) \tag{2}$$

Given a force F applied on the top of the pulse shape as Fig.1, the deformed curve can be calculated as:

$$B_{LD} = C_{TD}(F, TC\,(T_{LA}, T_{LB}, T_{LC})) \tag{3}$$

B_{LD} can be discretized as a pointset

$$B_{LDP} = \{P_{LD}\,(i)\,|\mathrm{i} = 0..\mathrm{n}\} \tag{4}$$

The stress at each point in B_{LDP} can be described as:

$$\sigma_{LDP} = \{\sigma_{LD}\,(i)\,|\mathrm{i} = 0..\mathrm{n}\} \tag{5}$$

And the strain of each point can be described as:

$$\varepsilon_{LDP} = \{\varepsilon(i)|\mathrm{i} = 0..\mathrm{n}\} \tag{6}$$

Considering the curve as the centre line of a beam printed by conductive materials, the changes of the resistance is

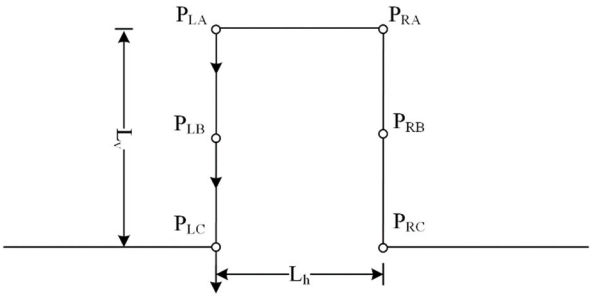

(a) The initial rectangular pulse shape

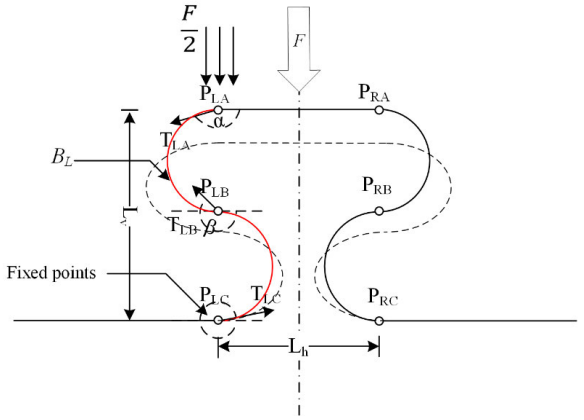

(b) The initial condition for the geometry optimization

FIGURE 1. Geometric profile of the sensor.

correlated with the strain introduced by F. To maximize the changes of the resistance, we defined a term as

$$SUM_{\varepsilon} = \sum_{i=0}^{n} (\varepsilon_{LDP}(i)) \tag{7}$$

to reflect the electronics requirements. Meanwhile, a uniform stress distribution prevents localized stress concentrations that might lead to uneven deformation and potential destruction of the structure. To maintain as uniform as possible stress distribution along the curve B_{LD}, we introduce a new term to reflect the structural requirements as:

$$STD_{\varepsilon} = STD(\sigma_{LDP}) \quad \forall \max(\sigma_{LDP}) < 2/3\sigma_y \tag{8}$$

where STD stands for standard deviation, σ_y is the yield strength of the material and $2/3$ is a safety factor.

T_{LA}, T_{LB}, T_{LC} can be found by maximizing Eq.7 while minimizing Eq.8. A cost function is then formulated, and T_{LA}, T_{LB} and T_{LC} can be found by minimizing the cost function as:

$$T_{LA}, T_{LB}, T_{LC} = argmin(STD_{\varepsilon} - \lambda SUM_{\varepsilon}) \tag{9}$$

B_L in Eq.2 can be defined based on the found T_{LA}, T_{LB} and T_{LC}, and due to the symmetry of the design, curve B_R at the right side of the design can be acquired by mirroring B_L regarding the centre line.

The proposed approach was implemented in Rhino® Grasshopper® [27]. Eq.3 was executed with the assistance of Karamba 3D [28]. A genetic algorithm was employed to determine the values of T_{LA}, T_{LB} and T_{LC} as in Eq.9. Figure 2 presents the curve B_L and B_{LD} before and after the optimization regarding both unloaded and loaded conditions, respectively. In the loaded condition, we imprinted the value of stress (Eq. 5) as the colour of the curve. It can be observed that after optimization, when a force of 15N is applied, the deformation of the sensor profile, primarily in blue, is significantly greater than that of the initial design under the loaded condition, which is mainly in purple. Furthermore, the maximum stress (100 Kpa) remains well below the yield strength (σ_y) of 3D printed Polylactic acid (PLA, worst case $\sigma_y \approx 6.71$ Mpa as [29]).

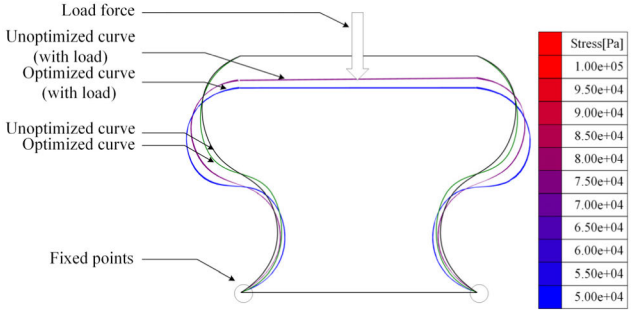

FIGURE 2. Stress distribution before and after optimization (Unit: Pascal).

Based on the optimized contour, the solid form of the sensor is obtained through two steps:1) Extruding the 2D profile into a 3D surface, extending it by a distance W; 2) Thickening the extruded surface on each side by an amount of $T/2$ as Fig.3. In this context, W represents the width of the structural electronics sensor, and T represents its thickness. Notably, considering the manufacturing method, in this case Fused Deposition Modelling (FDM), we have specified that T is the product of a positive integer and the nozzle diameter, e.g. $T = 0.8\,mm = 2 * 0.4\,mm$, where $0.4\,mm$ is the diameter of the extrusion nozzle.

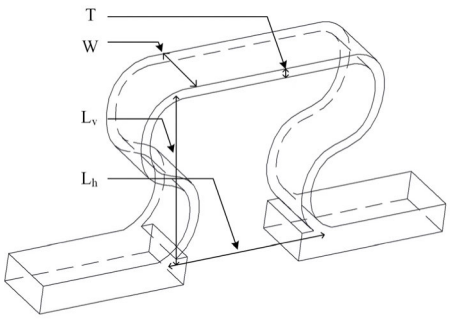

FIGURE 3. 3D view of a sensor.

III. SENSOR FABRICATION

The filament's composition consists of a blend of Polylactic Acid (PLA) and carbon black, which offers higher

stiffness and volumetric resistivity compared to conductive Thermoplastic Polyurethane (TPU). A conductive filament from Proto-Pasta was employed in fabricating the sensor. The filament's composition consists of a blend of Polylactic Acid (PLA) and carbon black. While the mechanical properties are similar to 3D printed PLA [29], the 3D-printed part also displays anisotropic volume resistivities. In the direction along the extrusion, the volume resistivity is about 0.3 Ohm·m, whereas in the z-direction (against layers), it measures 1.15 Ohm·m [21]. The glass transition temperature (Tg) for PLA is approximately 55°C [30].

(a) The printing process for the sensors

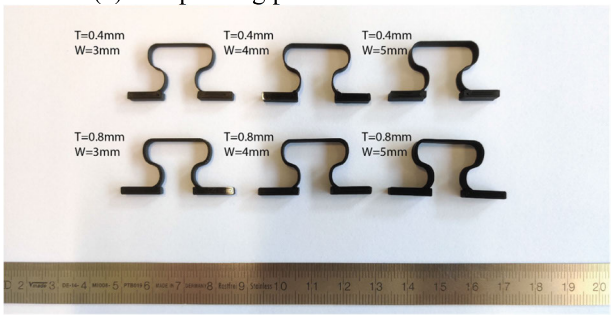

(b) Printed sensors

(c) Sensor connected with wires (top view)

FIGURE 4. 3D printed sensors.

Six variations of force sensors were designed. While all sensors have the same height (H = 25.4 mm, 1 inch), the width W has three configurations: 3, 4 and 5 mm, and the thickness T has two configurations: 0.4 mm and 0.8 mm. Printing was carried out using an Ultimaker® 5, with a nozzle size of 0.4mm and the nozzle temperature maintained at 215°C. The layer height was set as 0.15 mm, and the bed temperature was 60°C. Since the thickness of the sensor does not exceed 2.4 mm, the entire structure is sliced to multiple contours. For each of the 6 types of sensors, 3 identical copies were printed. The printing process for these sensors is illustrated in Fig.4(a), and the printed 6 types of sensors are shown in Fig.4(b). The printing time for a single sensor was approximately 12 minutes.

Cables were connected to the left and right ends of each sensor, respectively as Fig.4(c). A support structure, which was printed by dielectric PLA (white part in Fig.4(c)), were used to fix the "bottom" of the sensor to avoid any displacement in the loading/unloading process. The infilled density was set to 100% with Y-layering to minimize the contact resistance [30]. Additionally, the thickness of the connection part of the sensor was increased to reduce the resistance. Copper wires were heated and inserted into the structure to ensure a relatively consistent contact surface.

IV. SENSOR CHARACTERISTICS

In this section, we present the outcomes of a series of experiments aimed at investigating the sensor's performance. First, we describe the loading/unloading experiment, which was conducted to examine the accuracy, the sensitivity and part-to-part differences of the sensors [31]. Subsequently, the printed sensors were placed in a climate chamber to assess the influence of environmental temperature and humidity on the sensors' outputs.

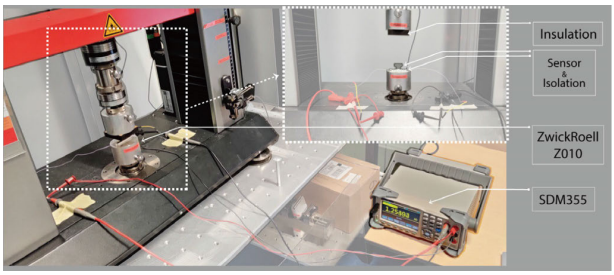

FIGURE 5. Setup of the loading/unloading experiment.

A. LOADING AND UNLOADING

Figure 5 shows the setup of the loading/unloading experiment, a tensile testing machine Zwick/Roell Z010 [32] was used to control the displacement applied to the sensor, and a SDM355 digital multimeter, was used to measure the resistance. The environment temperature was about 20°C. To reduce the effect of the contact resistance, a four-wire measurement technique was employed to eliminate contact resistances in the experiment's measurement [32]. Sensors with different parameters have different behaviours. Figure 6 shows the deformation of 6 sensors with different parameters regarding the load. For deformations, the mean maximum displacement of the three 0.8mm-thickness samples was 1.88mm, and for the three 0.4mm-thickness samples, it was 4.06mm. Regarding the maximum loads of 0.8mm-thickness sensors, for 3, 4, and 5mm-width sensors, the mean values were 11.67, 14.10, and 18.00N, respectively. For 0.4mm-thickness samples, they were 2.09, 2.81 and 3.37N, respectively. Here, thickness played a major role on the performance of the sensor. Based on these results, we controlled the deformation (displacement) between 0 and 1.25mm for

0.8mm-thickness samples and between 0 and 2.5mm for 0.4mm-thickness sensors in the following experiments. With this setup, the introduced working strain ranges from 0% to 5% (maximum) for 0.8mm-thickness samples and from 0% to 10% (maximum) for 0.4mm-thickness samples. The introduced strain ranges from 0% to 5% (max) for 0.8 mm thickness samples and 0% to 10% (max) for 0.4mm thickness. For each of the 6 types of sensors, three identical copies were evaluated for 100 compression cycles, and the force and resistance were documented.

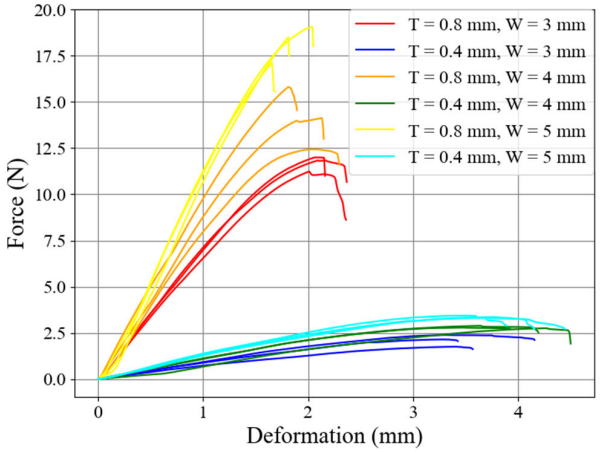

FIGURE 6. The maximun working range of sensors.

The resistance of the sensor during the first 100 cycles is presented in Fig.7(a). It can be observed that the resistance changes with the applied displacement (and force) during the initial cycles. However, the range and the mean value of each cycle gradually decrease until the 70th cycles. Figure 7(b) shows the relationship between the measured force and resistance for the 1st, 70th, and 100th cycles. As we used the same displacement in each cycle, in the initial cycles, the resistance ranges from 2650 Ω (no force) to 2690 Ω (∼7 Newton). In the 70th and 100th cycles, the resistances consistently changed between 2620 Ω (no force) and 2645 Ω (∼6 Newton). This phenomenon can be caused by the gradual stabilization of the 3D printed sensor's state, which is reflected in the reduced range of resistance and force [33].

To characterize the response of the sensor in the stable state, the relative change of the resistance, i.e. $\Delta R/R$, was used as the response of the measured force. The outputs of the 6 types of sensors are presented Fig.8(a). In the figure, it can be found that the sensors exhibit asymmetrical responses between the loading and unloading directions, resulting in crescent-like response curves. The asymmetry between loading and unloading might be attributed to resistance hysteresis, a nonlinearity frequently observed in phase-change materials [34].

Most sensors achieved 1% changes regarding the resistance and the sensor with T = 8mm, and W = 5mm reached 1.6%. Furthermore, an observation is that the width of the loops reduces as the size of the sensor decreases (from right to

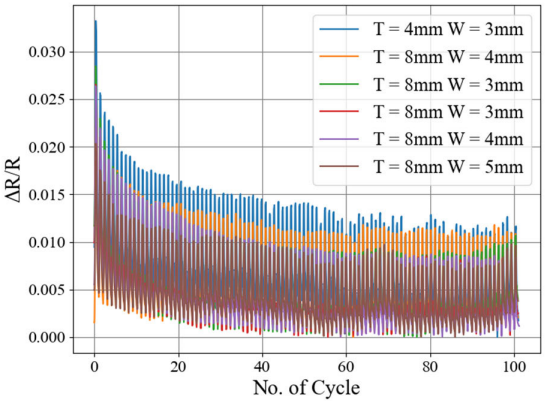

(a) The resistance of a sensor of 100 cycles

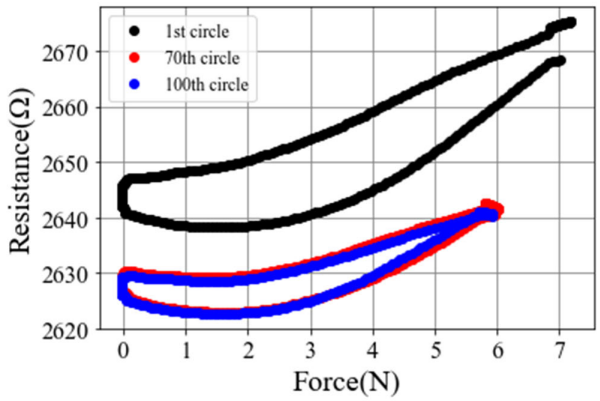

(b) The relations between force and resistance of a sensor (Width = 3mm, Thickness = 0.8mm) in 100 cycles

FIGURE 7. Resistances of a sensor during loading and unloading process.

left as Fig.8(a)). Considering the noise at the beginning/end of the loading/unloading situation, we specified a working range (as the window) as Fig.8(b) to establish monotonic relations between $\Delta R/R$ and the applied force.

Using the defined working range, we explored the range, the accuracy, and the part-to-part difference among different prints of each type of sensors. The results are presented in Fig.9 where the horizontal axis is $\Delta R/R$, the vertical axis is the force, and the error bar indicated the variations of 3 identical prints, each 30 cycles. Overall, the sensor's performance remains consistent. However, it's noteworthy that in certain designs (Fig. 9(c) and 9(f)), the part-to-part differences become larger as the applied forces increase.

The range of the sensors, the root mean square error (RMSE), and part-to-part variations are presented in Table 1. Column A in Table 1 shows the mean RMSE of each type of sensor in 30 cycles as Eq.10.

$$A = \frac{\sum_{i=1}^{3} \sqrt{\frac{\sum_{i=1}^{n} \left(f_i - \hat{f}_i\right)^2}{n}}}{3} \tag{10}$$

where f_i is the actual measured force, $\hat{f}_i$ is the estimated force within the individual sensors. Within the range of each type of

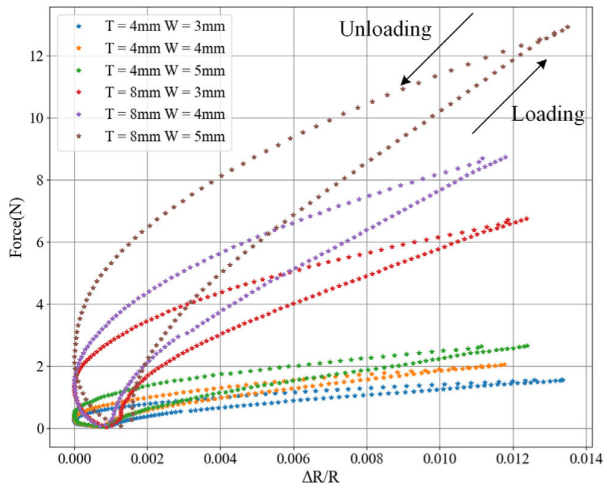

(a) Sensor load/unload graphs regarding $\Delta R/R$ and force

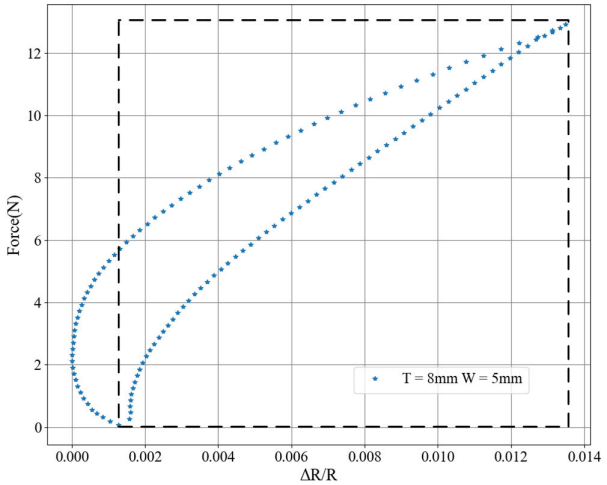

(b) The proposed working range for characterizing the performance of sensors

FIGURE 8. Overview of the performance of the sensors.

TABLE 1. RMSE and standard deviations of accuracy (A) and RMSE of part-to-part difference (P) regarding ΔR/R.

T	W	L/U	Range (N)	A	%	P	%
0.4	3	L	0.578-1.453	±0.011	1.26	±0.029	3.31
0.4	4	L	0.839-1.997	±0.032	2.76	±0.041	3.54
0.4	5	L	0.983-2.325	±0.021	1.56	±0.066	4.92
0.8	3	L	2.076-6.248	±0.03	0.72	±0.1	2.4
0.8	4	L	2.599-7.954	±0.025	0.47	±0.121	2.26
0.8	5	L	3.69-11.574	±0.173	2.19	±0.279	3.54
0.4	3	U	0.515-1.399	±0.012	1.36	±0.021	2.38
0.4	4	U	0.794-1.956	±0.033	2.84	±0.053	4.56
0.4	5	U	0.887-2.249	±0.019	1.4	±0.06	4.41
0.8	3	U	1.784-5.931	±0.057	1.37	±0.124	2.99
0.8	4	U	2.303-7.588	±0.054	1.02	±0.122	2.31
0.8	5	U	3.387-11.181	±0.1	1.28	±0.12	1.54
			MEAN±STD		1.52±0.7		3.18±1.01

sensors, the overall mean accuracy is 1.52% and the standard deviation is 0.7%. The P column in Table 1 shows part-to-part variations of each type of sensors, which is the RMSE of all sensors (30 cycles). The mean part-to-part variation is 3.18% and the standard deviation is 1.01%.

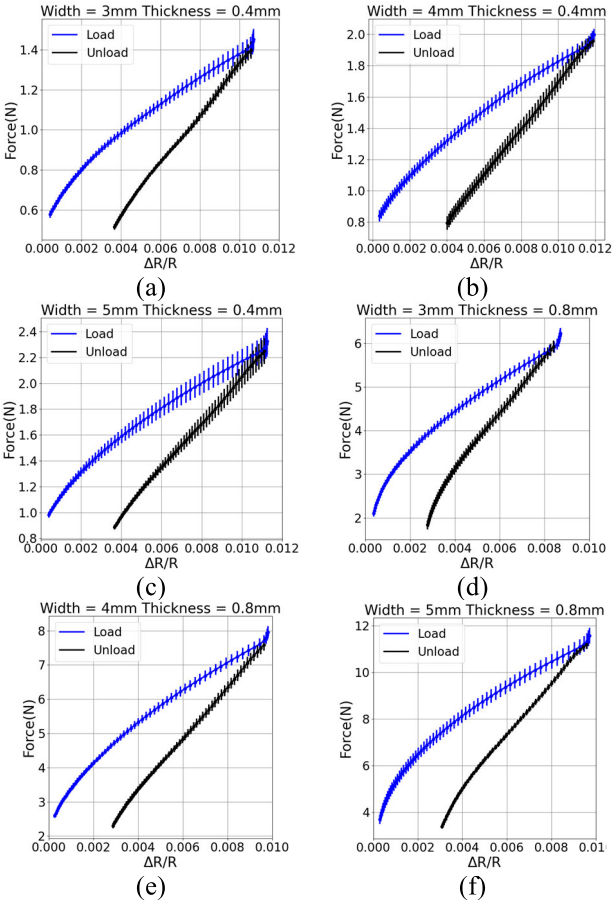

FIGURE 9. Relations between $\Delta R/R$ and the force.

As all sensors exhibits linear behaviour in the loading and unloading process within the working range, we made a linear regression of the loading and unloading process of each type of sensors as presented in Fig.8. In the regression, the $\Delta R/R$ is used as a predictor and the force is used as the responsible variable, as in the usage scenario of force sensors. Parameter a is the sensitivity and b is the residual.

$$Force = a\Delta R/R + b \tag{11}$$

Table 2 presents the results of the linear regressions. All R^2 value are above 0.95, which show the strongly linearity of the response of the sensors. All p values are at the significance levels. The sensitivity (a) of thicker and wider sensors are higher than thinner and narrower ones.

B. TEMPERATURE AND HUMIDITY

The effects of environmental temperature and humidity on the sensors were investigated using an ESPEC SH-661 temperature & humidity chamber as Fig.10(a). In the experiment, we adjusted the temperature from 10°C to 25°C at 5°C step, as the temperature of glass transition (Tg) for PLA is

TABLE 2. The parameters of regression equations (T-Thickness of sensors, W- Width of sensors, L/U – Loading/Unloading).

T	W	L/U	a	b	R^2	p
0.4	3	L	77.919	0.635	0.982	<0.01
0.4	4	L	93.807	0.907	0.991	<0.01
0.4	5	L	112.603	1.081	0.97	<0.01
0.8	3	L	474.866	2.531	0.982	<0.01
0.8	4	L	521.656	2.981	0.988	<0.01
0.8	5	L	754.456	4.623	0.976	<0.01
0.4	3	U	120.521	0.111	0.98	<0.01
0.4	4	U	141.196	0.266	0.984	<0.01
0.4	5	U	171.647	0.316	0.968	<0.01
0.8	3	U	749.12	0.289	0.989	<0.01
0.8	4	U	949.347	0.343	0.989	<0.01
0.8	5	U	1148.374	0.35	0.99	<0.01

approximately 56°C. For the relative humidity, we varied it from 30% to 90% at a step of 15%.

Three repetitive tests were conducted where for each round, we started from 10°C and 30% relative humidity. The testing results are presented in Fig.10(b) and Fig.10(c), respectively. Table 3 shows the mean and standard deviation of $\Delta R/R_0$ on the temperature and the relative humidity at each configuration. Here R_0 is the initial resistance of the sensor (10°C, 30% relative humidity).

TABLE 3. The drift on humidity and temperature.

	30%	45%	60%	75%	90%
10°C	0	0.001 ±0.001	0.002 ±0.001	0.004 ±0.001	0.006 ±0.002
15°C	0.044 ±0.001	0.045 ±0.002	0.046 ±0.001	0.049 ±0.002	0.053 ±0.003
20°C	0.088 ±0.001	0.091 ±0.004	0.091 ±0.001	0.094 ±0.002	0.1 ±0.004
25°C	0.148 ±0.003	0.15 ±0.004	0.154 ±0.005	0.159 ±0.004	0.171 ±0.006

Experiment results indicates that both temperature and humidity influence the $\Delta R/R_0$, however, at different amplitudes. As the 3D printing filaments are hygroscopic, they can absorb moisture from the air, which might be the reasons of the changes of $\Delta R/R_0$ regarding the relative humidity. For instance, at 10°C, the change of $\Delta R/R_0$ is 0.006 while the humidity changes from 30% to 90%. For the temperature, $\Delta R/R_0$ changes from 0 to 0.17, mainly caused by thermal expansion [35]. To minimize the influence of the temperature and the relative humidity, we developed a regression equation to compensate as Eq.11, where the humidity (H) and the temperature (T) are used as a predictor and $\Delta R_c/R_0$ is the compensation.

$$\Delta R_c/R_0 = a + bH + cT + dH^2 + eT^2 + fHT + gH^3 + hT^3 + iH^2T + jHT^2 \quad (12)$$

(a) Sensors in the climate chamber

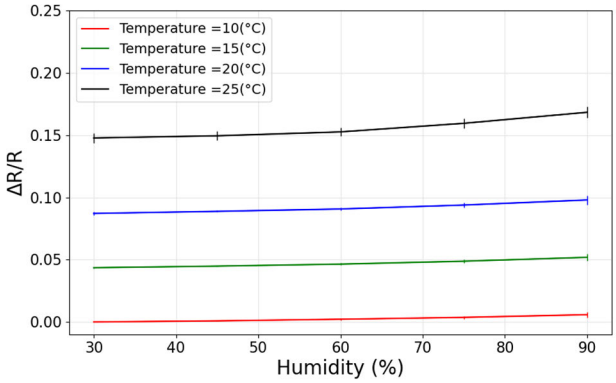

(b) The effect of humidity on $\Delta R/R$

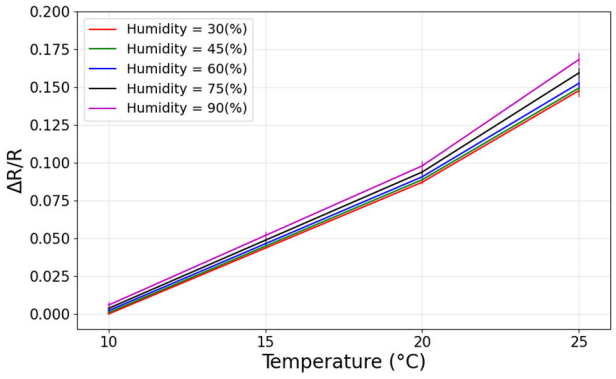

(c) The effect of temperature on $\Delta R/R$

FIGURE 10. Characterizing the influence of Temperature and humidity on the sensor.

Table 4 presents the values of the coefficient in Eq.12. Within the working temperature range (10°C-25°C and 30%-90%), the accuracy of the temperature compensation (RMSE) is ±0.001 ($R^2 = 0.998$), which is comparable to the characteristics of other force sensors [36], [37].

V. DISCUSSION

In contrast to an experimental approach in sensor design, we have introduced a novel computational approach that considers both mechanical and electronic properties in the early stage of sensor design. A set of force sensors was

TABLE 4. Polynomial regression for humidity and temperature compensation (10∼25°C and 30∼90%).

a	-1.825×10^{-1}
b	6.555×10^{-4}
c	2.697×10^{-2}
d	-4.959×10^{-6}
e	-1.164×10^{-3}
f	-5.655×10^{-5}
g	1.197×10^{-8}
h	2.461×10^{-5}
i	3.016×10^{-7}
j	1.023×10^{-6}

designed and manufactured using 3D printing techniques. Compared to traditional force sensors, these 3D printed electronic force sensors integrate both mechanical and electronic functionalities, reduce manufacturing costs, and thereby have the potential to enhance the overall system efficiency.

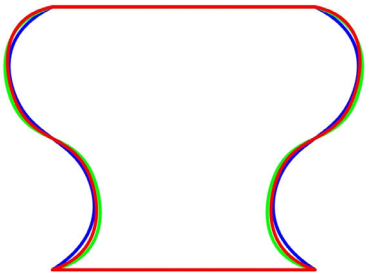

(a) Optimized geometric profiles with different λ

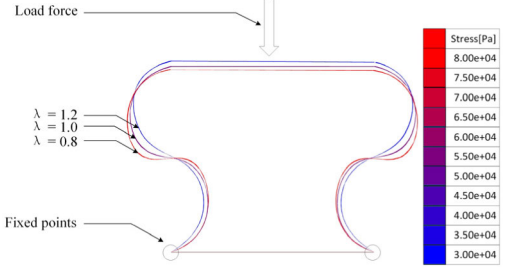

(b) Stress distribution and deformation of the sensor with different λ

FIGURE 11. The influence of λ.

A. THE VALUE OF λ

In the cost function for optimizing sensor shape, we introduced the parameter λ to balance the needs of uniform stress and large strain, with the goal of enhancing both mechanical and electronic properties. Within the same geometric envelope and boundary conditions, modifying the parameter λ allows for tailoring the sensor's behaviour to meet specific requirements. Figure 11 shows the deformation and stress of the sensor profile under the same load regarding $\lambda = 0.8$, 1, and 1.2, respectively. A larger λ might introduce increased deformability, resulting in higher sensitivity. Conversely, when λ is small, the sensor prioritizes stress uniformity, expanding its operating range while maintaining robustness against applied forces.

B. SENSOR CHARACTERISTICS

Given that the environment temperature and humidity introduce a large portion of errors, we introduce a humidity and temperature compensation mechanism to improve the accuracy of the sensors. However, temperature and relative humidity sensors are always needed for the compensation.

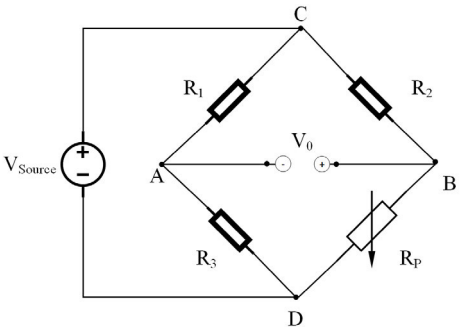

FIGURE 12. A Wheatstone-bridge-based readout circuit for temperature and humidity compensation.

Another possible solution is to introduce a Wheatstone bridge in the readout circuit to reduce the influence of temperature and humidity as Fig.12. In the figure, R_P is the proposed force sensor, R_1, R_2 and R_3 are resistors made of the same materials and manufacturing methods with the same (or similar) resistance. The relationship between the R_P and the voltage of the bridge V_0 can be denoted as:

$$V_0 = \left(\frac{R_P}{R_2 + R_P} - \frac{R_3}{R_1 + R_3} \right) \cdot V_s \tag{13}$$

where V_s is the source voltage.

Assuming the resistances of R_1, R_2 and R_3 and R_P are denoted as $R + \Delta R_{TH}$ Ω, where ΔR_{TH} are the change of resistance introduced by the temperature and the relative humidity. When an external force F is applied on R_P, the resistance of R_P is changed to $R + \Delta R_{TH} + \Delta R_F$, where ΔR_F is introduced by the force. Based on Eq.13, $\Delta R_{TH}/R$, which is the error introduced by the environmental temperature and relative humidity, can be calculated as:

$$\frac{\Delta R_{TH}}{R} = \frac{4V_0(1 + \Delta R_F/R)}{V_s - 2V_0} \tag{14}$$

In Table 3, errors introduced by the environmental temperature and the relative humidity span from 0 to 0.17. Given $V_s = 5V$ and the range of $\Delta R_F/R$ from 0 to 0.1 (as Fig.8), the maximum value of $\Delta R_{TH}/R$ calculated by Eq.13 is 0.0017. Though it is slightly larger than the error compensated by the temperature and humidity compensation equation (Eq. 11), it is 100 times smaller than the maximal error (0.17 as per Table 3) before compensation. Besides, temperature and humidity sensors are not needed using this approach, which is also an advantage.

C. DESIGN IMPLICATIONS

Although we only presented individual structural electronic sensors, similar sensors in various forms can also be designed and manufactured for different applications. Figure 13 illustrates a sensor array consisting of nine individual sensors. This sensor array can be utilized to measure the force applied to a surface, for example, as a smart cushion. Based on 3D printing techniques, sensors in the same vertical column can be manufactured simultaneously, saving time and effort while minimizing part-to-part differences. The information acquired from the 'sensor cells' can be read using a multiplexer sensor network. Besides, sensors in 3D shapes are also under exploration.

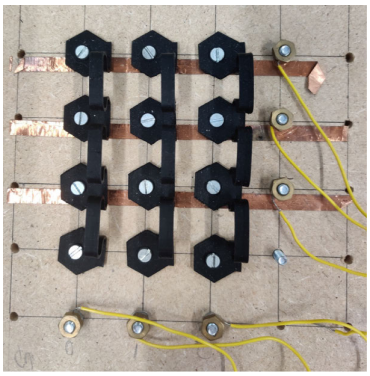

FIGURE 13. A printed sensor array system.

D. LIMITATIONS

The design exploration started with a combined tangent curve. However, alternative shapes for various applications, particularly those involving 3D design, were not investigated. Furthermore, by modifying the geometry of the sensing element, it may be possible to reduce hysteresis error and enhance stability over cyclic deformations [38]. The hysteresis partly results from mechanical properties and partly from the conductive material itself, which appears to be prone in printed conductive piezoresistive sensors [15]. It is a known problem as shown in other literatures [39], [40], [41]. The reasons might be the distribution of conductive materials in the microstructure, as well as other dynamics in the system [42]. These aspects will be further examined in our future work. Additionally, this study revealed that the impact of humidity on the changes of resistances was marginal, while temperature exhibited a significantly larger effect. During the study, the selection of materials was constrained by the limited availability of conductive filaments, particularly concerning their thermal properties. For instance, as Tg of PLA is 55°C, we limited the maximum temperature of the proposed sensors to 25°C to ensure that the sensor materials maintain their structural integrity and functionality during operation. Whether the relationship between the force and resistance changes of the sensor at different temperatures is consistent with that at 20°C needs to be further explored. Moreover, the 3D printing parameters, such as nozzle temperature, layer height and line with also affects the resistance, which are also to be further investigated [43]. Limited by the FDM printing technique, we printed the sensors following the W direction only as Fig.3 and Fig.4(a). Furthermore, future work will be conducted to characterize the behaviour of the sensor regarding fatigue and stability over time for a better understanding of the performance of the sensor. The utilization of new materials and multi-material printing with other printing techniques might trigger new opportunities for sensor designs as well. For example, conductive TPU offers high wear resistance, TPU molded components are less susceptible to cracking during operation. PLA displays inferior tear strength compared to TPU. On the other side, conductive TPU offers high mechanical elongation which is well suited for the implementation into elastomeric application.

VI. CONCLUSION

In this paper, we present an approach to design, manufacture and characterize structural electronics force sensors. With optimized geometric shapes, we printed the sensors utilizing conductive materials and FDM printing. The printed sensors are able to measure forces in the range of 0.5 (T = 0.4, W = 3mm) to 11.5 (T = 0.8, W = 5 mm) newtons with an overall accuracy about 1.52±0.7N. The mean part-to-part difference is 3.18%±1.01%. Humidity has little influence on the responses of the sensors. Though temperature might lead to drifting, after correction, the RMSE can be lowered to ± 0.001. Despite the limitations of using specific materials and FDM printing techniques, experiment results validate the proposed approach and highlight potential future opportunities for developing force sensors based on 3D printed structural electronics.

ACKNOWLEDGMENT

The authors would like to express their appreciation to Mascha Slingerland, Joris van Dam, Adrie Kooijman, and Martin Verwaal for their kind help during the experiment.

REFERENCES

[1] J. Fastier-Wooller, T. Dinh, V. Dau, H.-P. Phan, F. Yang, and D. Dao, "Low-cost graphite on paper pressure sensor for a robot gripper with a trivial fabrication process," *Sensors*, vol. 18, no. 10, p. 3300, Oct. 2018, doi: 10.3390/s18103300.

[2] L. Yuan and J. Li, "Smart cushion based on pressure sensor array for human sitting posture recognition," in *Proc. IEEE Sens.*, Oct. 2021, pp. 1–4, doi: 10.1109/SENSORS47087.2021.9639463.

[3] Y. Song, "Human digital twin, the development and impact on design," *J. Comput. Inf. Sci. Eng.*, vol. 23, no. 6, pp. 1–28, Aug. 2023, doi: 10.1115/1.4063132.

[4] L. Qiu, Y. Li, Y. Yu, A. Abu-Siada, Q. Xiong, X. Li, L. Li, P. Su, and Q. Cao, "Electromagnetic force distribution and deformation homogeneity of electromagnetic tube expansion with a new concave coil structure," *IEEE Access*, vol. 7, pp. 117107–117114, 2019, doi: 10.1109/ACCESS.2019.2923264.

[5] X. Wang, Y. Zhang, X. Zhang, Z. Huo, X. Li, M. Que, Z. Peng, H. Wang, and C. Pan, "A highly stretchable transparent self-powered triboelectric tactile sensor with metallized nanofibers for wearable electronics," *Adv. Mater.*, vol. 30, no. 12, Mar. 2018, Art. no. e1706738, doi: 10.1002/adma.201706738.

[6] H.-J. Qiu, W.-Z. Song, X.-X. Wang, J. Zhang, Z. Fan, M. Yu, S. Ramakrishna, and Y.-Z. Long, "A calibration-free self-powered sensor for vital sign monitoring and finger tap communication based on wearable triboelectric nanogenerator," *Nano Energy*, vol. 58, pp. 536–542, Apr. 2019, doi: 10.1016/j.nanoen.2019.01.069.

[7] T. Seesaard and C. Wongchoosuk, "Flexible and stretchable pressure sensors: From basic principles to state-of-the-art applications," *Micromachines*, vol. 14, no. 8, p. 1638, Aug. 2023, doi: 10.3390/mi14081638.

[8] Z. H. Warsi, S. M. Irshad, F. Khan, M. A. Shahbaz, M. Junaid, and S. U. Amin, "Sensors for structural health monitoring: A review," in *Proc. 2nd Int. Conf. Latest Trends Electr. Eng. Comput. Technol. (INTELLECT)*, Nov. 2019, pp. 1–6, doi: 10.1109/INTELLECT47034.2019.8955453.

[9] J. Hu, G. Dun, X. Geng, J. Chen, X. Wu, and T.-L. Ren, "Recent progress in flexible micro-pressure sensors for wearable health monitoring," *Nanosc. Adv.*, vol. 5, no. 12, pp. 3131–3145, Jun. 2023, doi: 10.1039/d2na00866a.

[10] R. Das. *Structural Electronics 2017–2027: Applications, Technologies, Forecasts*. IDTechEx. Accessed: Aug. 21, 2023. [Online]. Available: https://www.idtechex.com/en/research-report/structural-electronics-2017-2027-applications-technologies-forecasts/489

[11] Y. Song and R. A. Boekraad, "3D printed electronics: Opportunities and challenges from case studies," in *Proc. ASME Int. Design Eng. Tech. Conf. Comput. Inf. Eng. Conf.*, 2017, pp. 1–11. [Online]. Available: https://asmedigitalcollection.asme.org/IDETC-CIE/proceedings-abstract/IDETC-CIE2017/58110/259157

[12] T. Hou, J. Xu, W. S. Elkhuizen, C. C. L. Wang, J. Jiang, J. M. P. Geraedts, and Y. Song, "Design of 3D wireless power transfer system based on 3D printed electronics," *IEEE Access*, vol. 7, pp. 94793–94805, 2019, doi: 10.1109/ACCESS.2019.2928948.

[13] M. Ntagios, H. Nassar, A. Pullanchiyodan, W. T. Navaraj, and R. Dahiya, "Robotic hands with intrinsic tactile sensing via 3D printed soft pressure sensors," *Adv. Intell. Syst.*, vol. 2, no. 6, Jun. 2020, Art. no. 1900080, doi: 10.1002/aisy.201900080.

[14] G. L. Goh, G. D. Goh, V. P. Nguyen, W. Toh, S. Lee, X. Li, B. D. Sunil, J. Y. Lim, Z. Li, A. K. Sinha, W. Y. Yeong, D. Campolo, W. T. Chow, T. Y. Ng, and B. S. Han, "A 3D printing-enabled artificially innervated smart soft gripper with variable joint stiffness," *Adv. Mater. Technol.*, vol. 8, no. 24, Oct. 2023, Art. no. 2301426, doi: 10.1002/admt.202301426.

[15] A. Dijkshoorn, P. Werkman, M. Welleweerd, G. Wolterink, B. Eijking, J. Delamare, R. Sanders, and G. J. M. Krijnen, "Embedded sensing: Integrating sensors in 3-D printed structures," *J. Sensors Sensor Syst.*, vol. 7, no. 1, pp. 169–181, Mar. 2018, doi: 10.5194/jsss-7-169-2018.

[16] P. Laszczak, L. Jiang, D. L. Bader, D. Moser, and S. Zahedi, "Development and validation of a 3D-printed interfacial stress sensor for prosthetic applications," *Med. Eng. Phys.*, vol. 37, no. 1, pp. 132–137, Jan. 2015, doi: 10.1016/j.medengphy.2014.10.002.

[17] Y. Ni, R. Ji, K. Long, T. Bu, K. Chen, and S. Zhuang, "A review of 3D-printed sensors," *Appl. Spectrosc. Rev.*, vol. 52, no. 7, pp. 623–652, Aug. 2017, doi: 10.1080/05704928.2017.1287082.

[18] C. Bao, H. Moeinnia, T. Kim, W. Lee, and W. S. Kim, "3D structural electronics via multi-directional robot 3D printing," *Adv. Mater. Technol.*, vol. 8, no. 5, Mar. 2023, Art. no. 2201349, doi: 10.1002/admt.202201349.

[19] J. Xu, E. L. Doubrovski, J. M. P. Geraedts, and Y. Song, "Computational design for digitally fabricated 3D inductive power transfer coils," *J. Comput. Inf. Sci. Eng.*, vol. 22, no. 3, pp. 1–28, Jun. 2022, doi: 10.1115/1.4053500.

[20] H. Wei, X. Cauchy, I. O. Navas, Y. Abderrafai, K. Chizari, U. Sundararaj, Y. Liu, J. Leng, and D. Therriault, "Direct 3D printing of hybrid nanofiber-based nanocomposites for highly conductive and shape memory applications," *ACS Appl. Mater. Interfaces*, vol. 11, no. 27, pp. 24523–24532, Jul. 2019, doi: 10.1021/acsami.9b04245.

[21] *Electrically Conductive Filament*. Protoplant, makers of Protopasta. Accessed: Aug. 28, 2023. [Online]. Available: https://proto-pasta.com/collections/all/feature_electrically-conductive

[22] Q. Mu, L. Wang, C. K. Dunn, X. Kuang, F. Duan, Z. Zhang, H. J. Qi, and T. Wang, "Digital light processing 3D printing of conductive complex structures," *Additive Manuf.*, vol. 18, pp. 74–83, Dec. 2017, doi: 10.1016/j.addma.2017.08.011.

[23] Y. Zheng, X. Huang, J. Chen, K. Wu, J. Wang, and X. Zhang, "A review of conductive carbon materials for 3D printing: Materials, technologies, properties, and applications," *Materials*, vol. 14, no. 14, p. 3911, Jul. 2021, doi: 10.3390/ma14143911.

[24] J.-Y. Yoo, J.-S. Yang, M.-K. Chung, S.-H. Kim, and J.-B. Yoon, "A review of geometric and structural design for reliable flexible electronics," *J. Micromech. Microeng.*, vol. 31, no. 7, May 2021, Art. no. 074001, doi: 10.1088/1361-6439/abfd0a.

[25] E. S. O. Mata, G. S. C. Bermúdez, M. Ha, T. Kosub, Y. Zabila, J. Fassbender, and D. Makarov, "Printable anisotropic magnetoresistance sensors for highly compliant electronics," *Appl. Phys. A, Solids Surf.*, vol. 127, no. 4, p. 280, Mar. 2021, doi: 10.1007/s00339-021-04411-1.

[26] B. Guo, X. Ji, X. Chen, G. Li, Y. Lu, and J. Bai, "A highly stretchable and intrinsically self-healing strain sensor produced by 3D printing," *Virtual Phys. Prototyping*, vol. 15, no. sup1, pp. 520–531, Dec. 2020, doi: 10.1080/17452759.2020.1823570.

[27] *Grasshopper*. Grasshopper Algorithmic Modeling For Rhino. Accessed: Aug. 30, 2023. [Online]. Available: https://www.grasshopper3d.com/

[28] *Karamba3D*. Accessed: Aug. 24, 2023. [Online]. Available: https://karamba3d.com/

[29] J. A. Travieso-Rodriguez, R. Jerez-Mesa, J. Lluma, O. Traver-Ramos, G. Gomez-Gras, and J. J. Roa Rovira, "Mechanical properties of 3D-printing polylactic acid parts subjected to bending stress and fatigue testing," *Materials*, vol. 12, no. 23, p. 3859, Nov. 2019, doi: 10.3390/ma12233859.

[30] K. Sreekumar, B. Bindhu, and K. Veluraja, "Perspectives of polylactic acid from structure to applications," *Polym. Renew. Resour.*, vol. 12, nos. 1–2, pp. 60–74, Feb. 2021, doi: 10.1177/20412479211008773.

[31] G. Gattere, F. Rizzini, L. Corso, A. Alessandri, F. Tripodi, and I. Gelmi, "Experimental investigation of MEMS DRIE etching dimensional loss," in *Proc. IEEE Int. Symp. Inertial Sensors Syst. (INERTIAL)*, Mar. 2018, pp. 1–4, doi: 10.1109/ISISS.2018.8358123.

[32] Zwick/Roell. *AllroundLine*. Allroundline Universele Testmachine. Accessed: Aug. 28, 2023. [Online]. Available: https://www.zwickroell.com/nl/producten/statische-materiaaltestmachines/universele-testmachines-voor-statische-toepassingen/allroundline/

[33] P. F. Flowers, C. Reyes, S. Ye, M. J. Kim, and B. J. Wiley, "3D printing electronic components and circuits with conductive thermoplastic filament," *Additive Manuf.*, vol. 18, pp. 156–163, Dec. 2017, doi: 10.1016/j.addma.2017.10.002.

[34] M. Al-Rubaiai, T. Pinto, D. Torres, N. Sepulveda, and X. Tan, "Characterization of a 3D-printed conductive pla material with electrically controlled stiffness," in *Proc. ASME Conf. Smart Materials, Adaptive Structures Intell. Syst.*, Nov. 2017, Art. no. V001T01A003, doi: 10.1115/SMASIS2017-3801.

[35] I. Tirado-Garcia, D. Garcia-Gonzalez, S. Garzon-Hernandez, A. Rusinek, G. Robles, J. M. Martinez-Tarifa, and A. Arias, "Conductive 3D printed PLA composites: On the interplay of mechanical, electrical and thermal behaviours," *Composite Struct.*, vol. 265, Jun. 2021, Art. no. 113744, doi: 10.1016/j.compstruct.2021.113744.

[36] S. S. Kumat and P. S. Shiakolas, "Design, inverted vat photopolymerization 3D printing, and initial characterization of a miniature force sensor for localized in vivo tissue measurements," *3D Printing Med.*, vol. 8, no. 1, Jan. 2022, doi: 10.1186/s41205-021-00128-2.

[37] M. Liu, Y. Zhao, Y. Shao, Q. Zhang, and C. Liu, "3D printed force sensor with inkjet printed piezoresistive based strain gauge," in *Proc. IEEE SENSORS*, Oct. 2018, pp. 1–4, doi: 10.1109/icsens.2018.8589771.

[38] S. K. Dhinesh and S. K. K. Lakshmanan, "Sensitivity enhancement through geometry modification of 3D printed conductive PLA-based strain sensors," *Rapid Prototyping J.*, vol. 29, no. 9, pp. 1969–1983, Oct. 2023, doi: 10.1108/rpj-02-2023-0069.

[39] C. S. Boland, U. Khan, C. Backes, A. O'Neill, J. McCauley, S. Duane, R. Shanker, Y. Liu, I. Jurewicz, A. B. Dalton, and J. N. Coleman, "Sensitive, high-strain, high-rate bodily motion sensors based on graphene–rubber composites," *ACS Nano*, vol. 8, no. 9, pp. 8819–8830, Sep. 2014, doi: 10.1021/nn503454h.

[40] M. Borghetti, M. Serpelloni, E. Sardini, and S. Pandini, "Mechanical behavior of strain sensors based on PEDOT:PSS and silver nanoparticles inks deposited on polymer substrate by inkjet printing," *Sens. Actuators A, Phys.*, vol. 243, pp. 71–80, Jun. 2016, doi: 10.1016/j.sna.2016.03.021.

[41] H. Song, J. Zhang, D. Chen, K. Wang, S. Niu, Z. Han, and L. Ren, "Superfast and high-sensitivity printable strain sensors with bioinspired micron-scale cracks," *Nanoscale*, vol. 9, no. 3, pp. 1166–1173, Jan. 2017, doi: 10.1039/c6nr07333f.

[42] T. Pinto, C. Chen, C. Pinger, and X. Tan, "3D-printed liquid metal-based stretchable conductors and pressure sensors," *Smart Mater. Struct.*, vol. 30, no. 9, Jul. 2021, Art. no. 095005, doi: 10.1088/1361-665x/ac15a1.

[43] J. Beniak, L. Soos, P. Križan, M. Matus, and V. Ruprich, "Resistance and strength of conductive PLA processed by FDM additive manufacturing," *Polymers*, vol. 14, no. 4, p. 678, Feb. 2022, doi: 10.3390/polym14040678.

JUN XU received the M.S. degree in biomedical engineering from Shanghai University, China, in 2018. He is currently pursuing the Ph.D. degree with Delft University of Technology. His current research interests include 3D printed electronics and 3D wireless power transfer.

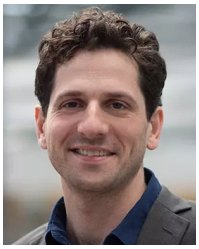

ZJENJA DOUBROVSKI received the Ph.D. degree from the Faculty of Industrial Design Engineering, Delft University of Technology. He is currently an Assistant Professor with the Department of Sustainable Design Engineering. His main research interests include multi-material AM, meta-materials, and smart mechanics.

MEHMET OZDEMIR received the Ph.D. degree in mechanical engineering from Politecnico di Milano. He is currently a Postdoctoral Researcher with the Faculty of Industrial Design Engineering. His main research interests include materials and design for digital fabrication, computational design, product personalization, and design methods and tools.

JO M. P. GERAEDTS received the Ph.D. degree in physics from Radboud University Nijmegen, in 1983. He joined Océ-van der Grinten N. V., in 1983. In 2008, he was appointed as the Chair of mechatronics design with the Faculty of Industrial Design Engineering, Delft University of Technology, and since then, he built step for step a new research environment for 3D multi-modal scanning, 3D multi-material printing, and human–robot interaction.

YU (WOLF) SONG (Member, IEEE) received the Ph.D. degree from the Department of Mechanical Engineering, The University of Hong Kong. He joined the Faculty of Industrial Design Engineering, Delft University of Technology, in 2001. He is currently an Associate Professor with the Department of Sustainable Design Engineering. His main research interests include human digital twins, 3D scanning, and Ergonomics.